Depth Analysis of Fe_2O_3-Incorporated Cobalt Synthesized via Gelatin-Modified Silica as Hard Template for Methylene Blue Photodegradation

Maria Ulfa* **and Istinganah Saetu Rohmah**

Chemistry Education Study Program, Faculty of Teacher Training and Education, Sebelas Maret University, Jl. Ir. Sutami 36A, Surakarta 57126, Indonesia

* ***Corresponding author:***

email: mariaulfa@staff.uns.ac.id

Received: June 11, 2025
Accepted: October 28, 2025

DOI: 10.22146/ijc.107799

Abstract: *The escalating occurrence of methylene blue (MB) contamination from textile wastewater underscores the urgent demand for effective photocatalytic remediation. This study presents a depth analysis of Fe_2O_3-incorporated cobalt photocatalysts synthesized using a gelatin-modified silica hard-template method, followed by calcination at 300 and 550 °C. Structural characterization via XRD, FTIR, and EDX confirmed enhanced crystallinity and Co–O phase formation at elevated temperatures, while BET analysis revealed a reduction in surface area (123.4 to 104.5 m^2/g) and pore volume (0.2236 to 0.1875 cm^3/g) due to sintering and template removal. FTIR data indicated the attenuation of hydroxyl and water-related bands, suggesting decreased surface hydration at higher temperatures. Despite the decline in surface metrics, α-Fe_2O_3–Co–550 exhibited superior photocatalytic efficiency, achieving greater than 90% MB degradation under visible light, attributed to an increased cobalt content (Fe:Co≈2:1), improved phase purity, and an optimized electronic structure. Kinetic modeling revealed pseudo-first-order behavior for both samples, with α-Fe_2O_3-Co-300 showing a higher rate constant ($K_1 = 0.01116\ min^{-1}$) yet lower overall degradation performance than α-Fe_2O_3-Co-550, highlighting the critical interplay of structural order, charge transfer efficiency, and compositional tuning enabled by hard-template synthesis for effective photocatalytic wastewater treatment.*

Keywords: *α-Fe_2O_3; cobalt; calcination temperature; photocatalyst; methylene blue*

■ INTRODUCTION

Water contamination caused by synthetic dyes, particularly methylene blue (MB), is a critical environmental issue due to its toxicity, chemical stability, and resistance to biodegradation [1-3]. MB, a common pollutant from the textile industry, hurts both aquatic ecosystems and human health [4-6]. Among various wastewater treatment technologies, semiconductor-based photocatalysis has emerged as an eco-friendly and efficient method for degrading organic contaminants under light irradiation [7-9].

Among various photocatalysts, α-Fe_2O_3 (hematite) is particularly attractive due to its chemical stability, low cost, abundance, and responsiveness to visible light [10-12]. However, its practical photocatalytic efficiency is severely limited by its narrow surface area, low charge carrier mobility, and high electron-hole recombination rates [13-15]. These challenges have motivated numerous modification strategies, including metal ion doping and nanostructuring, to enhance the material's optical and surface properties [16-17].

Cobalt (Co) doping has been demonstrated to enhance the photocatalytic activity of α-Fe_2O_3 by narrowing the band gap, increasing visible light absorption, and reducing electron-hole recombination [18-20]. Additionally, textural features, such as surface area and pore distribution, play a critical role in determining the interaction dynamics between pollutant molecules and active catalytic sites [19-21]. Nevertheless, optimizing these properties requires precise control over the material's morphology and structure during synthesis.

One promising approach to improving the textural characteristics of doped metal oxides is the use of hard templating techniques, particularly those utilizing silica matrices modified with biopolymers such as gelatin. Gelatin serves as a biodegradable structure-directing agent that can modulate pore formation during the sol-gel process, while silica provides a rigid scaffold to produce well-defined mesoporous frameworks [21-23]. This templated synthesis enables the formation of catalysts with tailored surface areas, porosities, and crystallite structures, which are crucial for photocatalytic activity.

Despite the known advantages of Co doping and template-assisted synthesis, few studies have investigated their combined effects, particularly when coupled with systematic variation of calcination temperature. Calcination temperature not only influences the removal of the organic template and the consolidation of the silica structure, but also governs crystallite growth, the degree of crystallinity, and the textural evolution of the metal oxide framework. At lower temperatures, higher surface area and smaller crystallites may be retained, whereas elevated temperatures enhance crystallinity at the expense of pore collapse or particle agglomeration [24-26]. Although prior studies have investigated either Co doping or calcination temperature independently in α-Fe_2O_3 systems, an integrative approach involving gelatin-templated silica frameworks remains [27-29]. variation of the calcination temperature aims to control the crystal size, degree of crystallinity, surface area, pore size distribution, and band gap energy of α-Fe_2O_3-Co, as explained in the previous studies, which showed a significant effect of calcination temperature on textural properties and photocatalytic activity [24,30].

This study addresses the current research gap by developing a novel Co-doped α-Fe_2O_3 photocatalyst synthesized via a gelatin-modified silica hard template, with systematic control of calcination temperature. The research aims to optimize photocatalytic degradation of MB by tailoring the textural and optical properties of the material, including surface area, pore structure, crystallinity, crystallite size, and band gap energy. The novelty lies in the synergistic integration of biopolymer templating, metal ion doping, and thermal treatment to produce high-efficiency photocatalysts. The expected outcomes of this work include the establishment of an optimal calcination protocol, a comprehensive understanding of structure–property–activity relationships in Co-doped α-Fe_2O_3 systems, and practical implications for designing advanced photocatalysts for textile wastewater remediation.

■ EXPERIMENTAL SECTION

Materials

The chemicals used in this study include iron(III) chloride hexahydrate ($FeCl_3 \cdot 6H_2O$, Sigma-Aldrich), iron(II) nitrate nonahydrate ($Fe(NO_3)_2 \cdot 9H_2O$, Sigma-Aldrich), cobalt(II) nitrate hexahydrate ($Co(NO_3)_2 \cdot 6H_2O$, Sigma-Aldrich), gelatin (technical grade, Sigma-Aldrich), Pluronic P123 ($EO_{20}PO_{70}EO_{20}$, Sigma-Aldrich), citric acid monohydrate ($C_6H_8O_7 \cdot H_2O$, Sigma-Aldrich), sodium hydroxide (NaOH, Sigma-Aldrich), methylene blue dye ($C_{16}H_{18}ClN_3S \cdot xH_2O$, Sigma-Aldrich), and distilled water (Smart-Lab). All reagents were of analytical grade and were used without further purification.

Instrumentation

The instruments used for characterizing the samples in this study include X-ray diffraction (XRD) from PANalytical (Model PW3050/60), operated within a 2θ range of 5° to 80°, to determine the crystallinity and phase composition of the synthesized materials. The surface area and porosity were measured using the Brunauer-Emmett-Teller (BET) method with a Quantachrome Nova 1200e instrument. Fourier-transform infrared spectroscopy (FTIR), performed using a Shimadzu 21 spectrometer with a resolution of 0.5 cm^{-1}, was employed to analyze functional groups in the materials in the wavenumber range of 300–4000 cm^{-1}. Energy-dispersive X-ray (EDX) analysis was conducted using a JEOL JSM-700 microscope at an accelerating voltage of 15 kV to examine the surface morphology and elemental composition of the samples.

Procedure

Synthesis of α-Fe_2O_3-Co

The Co-Fe photocatalyst was synthesized via a hard templating method using gelatin-modified mesoporous silica (SPG-20) as the template, followed by calcination and activation processes. The SPG-20 template was prepared by mixing Pluronic P123 and gelatin in a molar ratio of 1:0.4, followed by the dropwise addition of HCl solution and tetraethyl orthosilicate (TEOS) with a molar ratio of P123:TEOS = 1:11.5, stirred at 40 °C, then subjected to hydrothermal aging at 90 °C for 24 h. The solid was filtered, washed, oven-dried, and calcined at 550 °C to form SPG-20. This template was then activated by treatment with 0.1 M HCl for 24 h, followed by drying at 100 °C. For the synthesis of the Co-Fe photocatalyst, SPG-20 was used as a hard template, and metal precursors $Fe(NO_3)_3 \cdot 9H_2O$ and $Co(NO_3)_2 \cdot 6H_2O$ (ratio 2:1 and 3:1) were dissolved in water with a total metal-to-silica molar ratio of 1:1, stirred, and homogenized. Citric acid was added dropwise as a chelating agent in a molar ratio of 1:1 to the total metal content, followed by heating at 70 °C and drying at 100 °C. The resulting solid was calcined at two different temperatures (300 and 550 °C) for 5 h. The silica template was removed by treating the calcined solid with 2 M NaOH at 90 °C for 10 h, yielding the final Co-Fe photocatalyst.

Photodegradation of MB

The photocatalytic degradation of MB was carried out using a 0.2 L MB solution at a concentration of 2.0×10^{-5} kg/L. The initial pH of the solution was adjusted to 7.0 using 0.1 M HCl or NaOH, and the temperature was maintained at 25 ± 2 °C throughout the experiment. A total of 5.0×10^{-5} kg of the photocatalyst was added to the MB solution in an Erlenmeyer flask, followed by a 30-min dark adsorption period to achieve adsorption–desorption equilibrium. After equilibrium, the suspension was distributed into twelve dark glass vials, each containing 0.01 L of solution, and kept in dark conditions within the photocatalytic reactor. One vial was labeled C_0 (0 min) to represent the initial concentration before light irradiation. The remaining vials were placed on a shaker inside the reactor without caps. Photocatalytic degradation was initiated after 20 min by turning on the visible light source (a 300 W halogen lamp, λ = 400–700 nm) and the shaker to ensure uniform suspension. Samples were withdrawn at 5-min intervals up to 20 min, and subsequently at 10-min intervals until the 90th min. Each vial was immediately sealed after collection and stored in complete darkness to prevent further reaction. The concentration of MB in each sample was determined using a UV-vis spectrophotometer by measuring absorbance at 660 nm, which corresponds to the maximum absorption wavelength of MB.

■ RESULTS AND DISCUSSION

Photocatalyst Characterization

XRD analysis

The XRD patterns of α-Fe_2O_3–Co composites calcined at 300 and 550 °C confirm the influence of calcination temperature on crystallinity and phase composition. The characteristic reflections at $2\theta \approx 43°$, 53°, and 57° correspond to hematite (α-Fe_2O_3, JCPDS No. 00-024-0072), with slightly sharper and more intense peaks in the α-Fe_2O_3–Co-550 sample, indicating improved crystallinity (Fig. 1). In contrast, the broader reflections in α-Fe_2O_3–Co-300 suggest smaller crystallites, partial amorphous content, or possible lattice strain. The crystallite size values obtained from Scherrer analysis (Table 1) show only a minor increase from 4.52 to 4.75 nm, consistent with the limited crystal growth at moderate calcination temperature. Additional peaks at $2\theta \approx 65°$ are consistent with CoO (JCPDS No. 00-002-1217), becoming more pronounced at higher calcination temperatures, indicating the crystallization of cobalt oxide. This process is accompanied by the redistribution of Co^{2+} and Fe^{3+} cations between the tetrahedral (A) and octahedral (B) sites in the spinel cobalt ferrite (Fe_2O_3-Co) structure, which alters the magnetic interactions and magnetization values. Such redistribution, triggered by calcination temperature, modulates the magnetic properties, and saturation magnetization (Ms) and coercivity (Hc). Differences in cation distribution lead to variations in magnetic ordering

Table 1. Crystallite size of α-Fe_2O_3-Co samples calcined at 300 and 550 °C

Sample	D (nm)	Degree of crystallinity (%)
α-Fe_2O_3-Co-300	4.5219	5.2327
α-Fe_2O_3-Co-550	4.7542	6.1241

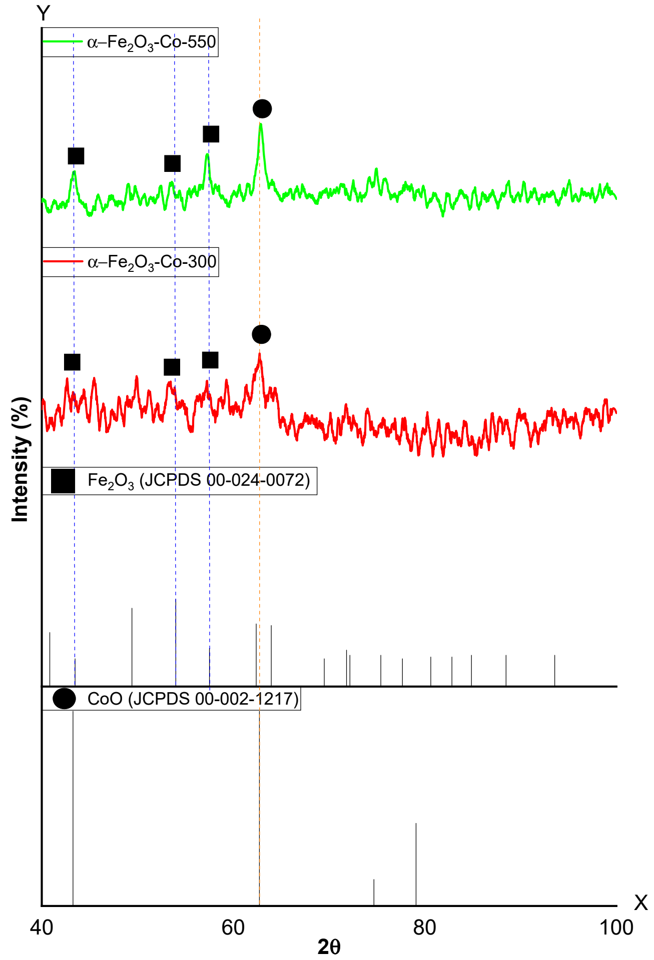

Fig 1. XRD patterns of α-Fe_2O_3-Co samples calcined at 300 and 550 °C

and Ms values, where higher calcination temperatures enhance crystallinity and change the cation distribution, thereby significantly influencing the magnetic properties. Although a full Rietveld refinement was not conducted in this study, future quantitative analysis will help elucidate the relative proportions of α-Fe_2O_3 and CoO. These observations confirm that calcination temperature plays a role in controlling crystallite growth, crystallinity, and phase evolution in the bimetallic oxide framework.

FTIR analysis

The FTIR spectra of α-Fe_2O_3–Co samples calcined at 300 and 550 °C provide insight into the structural and surface chemistry evolution induced by thermal treatment. Both spectra (Fig. 2 and Table 2) display characteristic absorption bands associated with the stretching and bending vibrations of surface hydroxyl groups, adsorbed water molecules, and metal–oxygen bonds, confirming the successful formation of bimetallic oxide structures. The broad absorption band observed in the range of 3373–3382 cm^{-1} is attributed to O–H stretching vibrations from surface hydroxyls and interlayer water molecules [31]. The intensity of this band significantly decreases with increasing calcination temperature, indicating the removal of physisorbed water and dehydroxylation at higher temperatures. A similar trend is observed at ~1632–1635 cm^{-1}, corresponding to the H–O–H bending mode of adsorbed molecular water, which further confirms the progressive

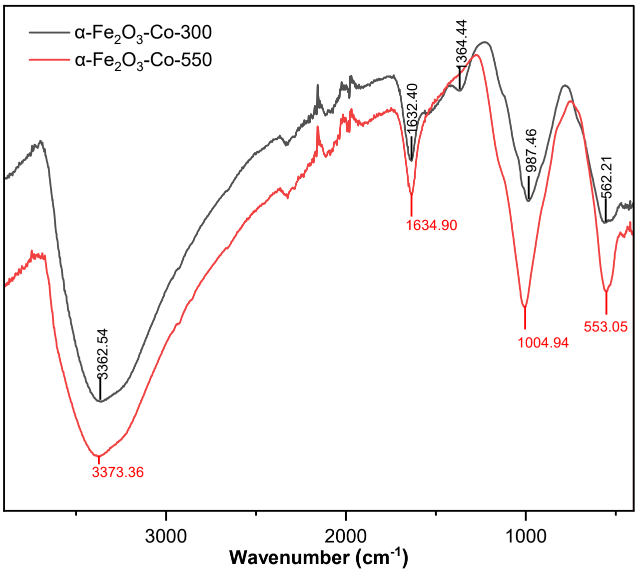

Fig 2. FTIR Spectra of α-Fe_2O_3-Co samples calcined at 300 and 550 °C

Table 2. FTIR band assignments and intensity of α-Fe_2O_3–Co–300 and α-Fe_2O_3–Co–550

Wavenumber (cm^{-1})	Functional group assignment	α-Fe_2O_3–Co–300 (black)	α-Fe_2O_3–Co–550 (red)	Relative change
3373–3382	O–H stretching	High intensity	Moderate intensity	Decreased
1632–1635	H–O–H bending (H_2O)	High intensity	Moderate intensity	Decreased
553–562	Fe–O/Co–O stretching	Moderate intensity	High intensity	Increased

dehydration of the material upon calcination at 550 °C.

Bands detected in the fingerprint region, particularly at ~1384 and ~987–1005 cm^{-1}, can be ascribed to residual nitrate species or organic remnants from precursors, which are substantially diminished in the α-Fe_2O_3–Co-550 sample. This suggests a more complete decomposition of the precursor materials and a cleaner oxide surface at higher calcination temperatures. More importantly, the absorption bands appearing at lower wavenumbers (553–562 cm^{-1}) are assigned to the Fe–O and Co–O lattice vibrations, which are indicative of metal–oxygen framework formation in the bimetallic oxide system [32]. These bands become more intense and better resolved in the α-Fe_2O_3–Co-550 spectrum, reflecting enhanced crystallinity and stronger metal–oxygen interactions as a result of the higher thermal treatment. Collectively, the FTIR analysis reveals that increasing the calcination temperature promotes the structural reorganization and condensation of metal–oxygen bonds, while concurrently removing volatile impurities and surface hydroxyl groups. This transformation contributes to the formation of a more ordered and thermally stable bimetallic oxide network, which is advantageous for applications such as catalysis, adsorption, or photocatalysis that demand robust material performance and high thermal stability.

Nitrogen adsorption–desorption analysis

The nitrogen adsorption–desorption analysis (Table 3 and Fig. 3) provides insight into the impact of calcination temperature on the textural properties of α-Fe_2O_3–Co bimetallic oxides. The nitrogen adsorption–desorption isotherms of the α-Fe_2O_3–Co samples (Fig. 3) exhibit type IV behavior with an H3 hysteresis loop, characteristic of mesoporous materials containing slit-like pores formed by particle aggregation. At 300 °C, the sample displays a high BET surface area of 123.445 m^2/g, BJH surface area of 107.101 m^2/g, a pore diameter of 5.03 nm, and a total pore volume of 0.2236 cm^3/g, reflecting a well-developed mesoporous network that favors dispersion of active sites. In contrast, calcination at 550 °C results in reduced adsorption capacity, surface area, and pore volume, which can be attributed to partial pore collapse and particle sintering. These results demonstrate a clear trade-off: while a higher calcination

Table 3. Porosity analysis of α-Fe_2O_3-Co samples calcined at 300 and 550 °C

Sample	BJH surface area (m^2/g)	BET surface area (m^2/g)	Pore diameter (nm)	Total pore volume (cm^2/g)
α-Fe_2O_3-Co-300	107.101	123.445	5.03228	0.2236
α-Fe_2O_3-Co-550	90.4514	104.526	3.60646	0.1875

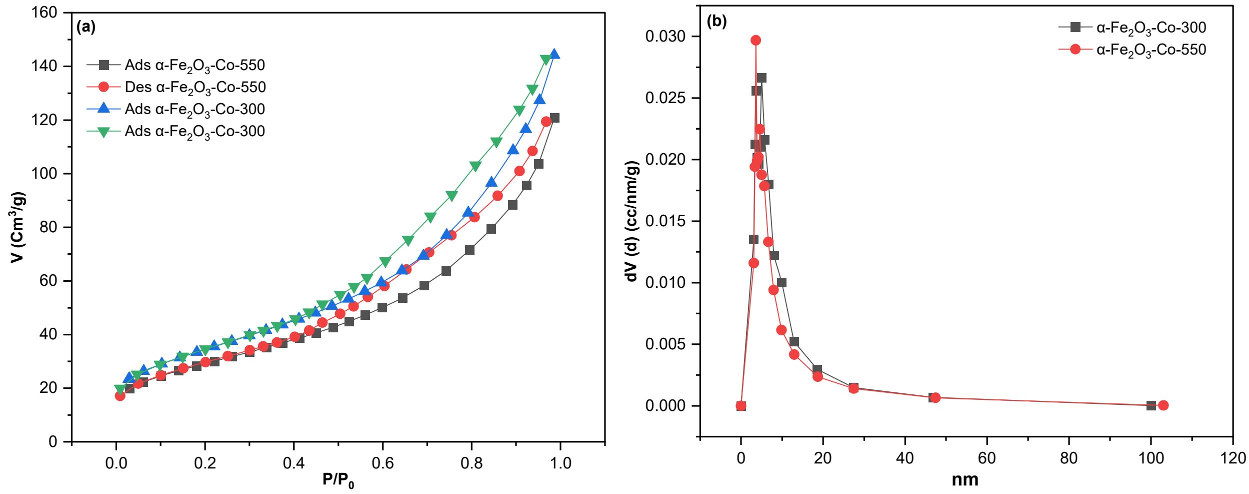

Fig 3. (a) Adsorption-desorption isotherm and (b) pore-size distribution of α-Fe_2O_3-Co-300 and α-Fe_2O_3-Co-550 samples

temperature enhances crystallinity and structural stability (as supported by XRD analysis), it simultaneously decreases the accessible surface area and porosity, potentially limiting the density of active sites available for photocatalytic reactions. Optimizing this balance between crystallinity and surface accessibility is therefore critical for maximizing catalytic performance.

Upon calcination at 550 °C, a marked decrease in both surface area and pore characteristics is observed. The BET surface area drops to 104.526 m^2/g, and the BJH surface area decreases to 90.451 m^2/g. Simultaneously, the average pore diameter reduces to 3.61 nm and the total pore volume diminishes to 0.1875 cm^3/g. These reductions are typically associated with partial sintering, pore collapse, or densification of the material matrix due to thermal treatment. The contraction in pore diameter and volume suggests that the elevated temperature promotes grain growth and coalescence of oxide particles, thereby reducing porosity and narrowing the pore network.

Despite the decrease, the material retains its mesoporous nature, as evidenced by the pore diameters remaining within the mesoporous range (2–50 nm). However, the decline in surface area and porosity may adversely affect the material's performance in applications where mass transport and surface reaction kinetics are critical. Therefore, a balance between sufficient thermal treatment for crystallization and preservation of mesostructural features is crucial in optimizing the performance of such bimetallic oxide systems.

UV-vis DRS analysis

Based on the UV-vis diffuse reflectance spectroscopy (DRS) data shown, the Tauc plots for α-Fe_2O_3-Co samples subjected to different calcination temperatures reveal slight variations in their optical band gap energies. The data indicate a notable decline in the band gap. Pure α-Fe_2O_3 possesses a band gap of 2.2 eV, while α-Fe_2O_3-Co-300 shows a gap of 1.773 eV (a reduction of 19.4%), and α-Fe_2O_3-Co-550 exhibits a gap of 1.180 eV (a reduction of 46.4%) (Fig. 4). This reduction aligns with studies indicating that cobalt doping in hematite can lower the band gap from approximately 2 eV to around 1.9 eV [33]. Additional research also verified that the band gap energy of Fe_2O_3 nanoparticles declines with the addition of Co as a doping material [34]. The incorporation of Co leads to significant alterations in the electronic configuration of Fe_2O_3. The research demonstrated that the inclusion of Co^{2+} in the Fe_2O_3 lattice was validated by the characterizations mentioned above. Incorporating Co into the α-Fe_2O_3 framework leads to a reduction in the band gap from 2.2 to 1.773 eV (at 300 °C). This phenomenon takes place as Co^{2+}/Co^{3+} ions substitute Fe^{3+} in the hematite crystal lattice, Co d orbitals generate extra energy levels within the band gap, and the interaction between Fe 3d and Co 3d orbitals alters the density distribution of electronic states [33].

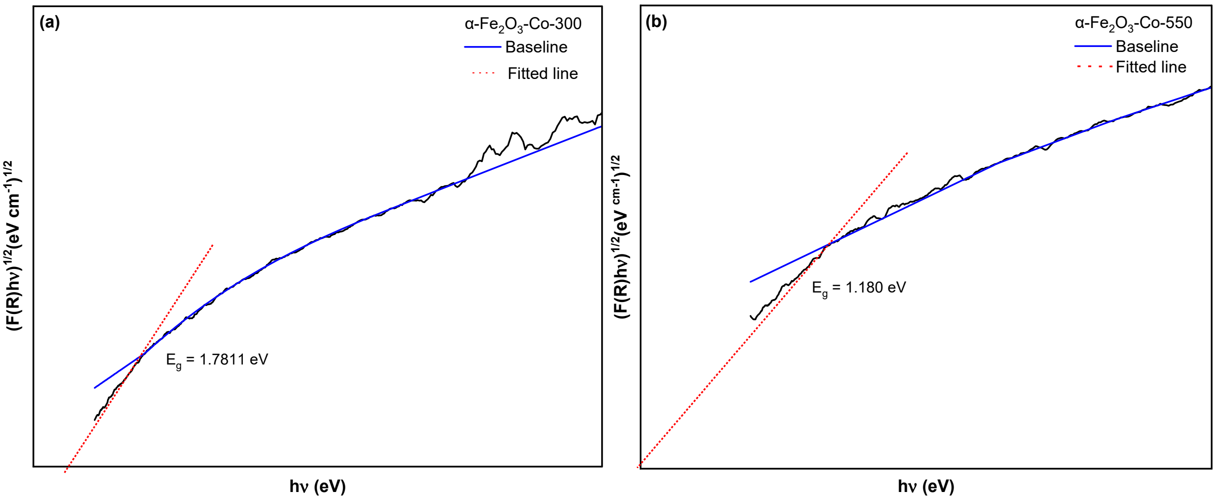

Fig 4. Band gap by Tauc plot of α-Fe_2O_3-Co samples at different calcination temperatures

Raising the calcination temperature from 300 to 550 °C led to a significant reduction in the band gap. This occurrence is backed by a study indicating that the reduction in band gap energy could result from enhanced crystallinity and larger particle size at higher calcination temperatures [35]. Elevated temperatures enhance the crystal framework and diminish imperfections [27]. The expansion or contraction of the crystal lattice influences the overlap of orbitals. The improved incorporation of cobalt into the host framework [35]. The 1.180 eV band gap in the sample calcined at 550°C enables photocatalytic activation using visible light. This aligns with the discovery that Co(5%)-Fe_2O_3 spindles show improved light absorption capacity and a red shift in the absorption edge [33].

The research demonstrated that Co-doped Fe_2O_3 spindles displayed superior catalytic degradation capabilities compared to single Fe_2O_3 spindles. This enhancement was a result of the inherent Co^{2+}/Co^{3+} redox cycling, which can speed up the interchange between Fe^{2+} and Fe^{3+}, boost the generation of •OH radicals for contaminant breakdown, and promote the movement of photoexcited charge carriers. The data acquired demonstrated alignment with the trend noted in existing literature. Previous research has indicated that the band gap energy for both undoped and Co-doped Fe_2O_3 nanoparticles at concentrations of 5, 10, 15, and 20 wt.% exhibits a gradual reduction, suggesting that the band gap energy diminishes as the cobalt content increases [34].

It is well established in the field of material science that elevated calcination temperatures typically result in an enhancement of the crystallinity of the synthesized material, which can be attributed to the increased energy and rearrangement of atomic structures within the crystal lattice [28-29]. Enhanced crystallinity is indicative of a more orderly arrangement of atoms within the crystal lattice, which can lead to improved material properties [36]. At elevated temperatures, particles typically undergo grain growth, leading to an increase in the size of the crystallites, which can significantly impact the physical and chemical properties of the material [37]. Furthermore, exposure to very high calcination temperatures may induce phase transitions, which can manifest as a transformation from an amorphous state to a crystalline state, or even shifts between different polymorphs, such as the transition from γ-Fe_2O_3 to α-Fe_2O_3 [38]. It is worth noting that high temperatures can lead to a reduction in the prevalence of structural defects, including oxygen vacancies, within the material, provided that the calcination process does not exceed certain thresholds. Excessive calcination, however, can paradoxically result in an increase in such defects [39-40].

In this study (Table 4), Tauc plots were constructed under the assumption of an indirect allowed transition, consistent with the commonly reported electronic structure of hematite-based systems. The observed narrowing of the band gap with Co incorporation and higher calcination temperature can be attributed to multiple contributing factors. First, the substitution of Fe^{3+} by Co^{2+}/Co^{3+} introduces additional electronic states within the band gap, thereby facilitating lower-energy electronic transitions. Second, the interaction between Fe 3*d* and Co 3*d* orbitals modifies the density of states near the conduction and valence bands, further reducing the effective band gap. Third, lattice strain induced by ionic size mismatch between Fe^{3+} (0.645 Å) and Co^{2+}/Co^{3+} (0.58–0.75 Å) perturbs orbital overlap and alters band dispersion. Additionally, the reduction in surface area and increase in crystallite size at elevated calcination temperature decrease the influence of surface defects and quantum confinement, thereby reinforcing

Table 4. Band gap energies of α-Fe_2O_3–Co samples at different calcination temperatures

Sample	Band gap (eV)	Reduction compared to pure α-Fe_2O_3 (%)	Transition assumption	Tauc plot equation*
Pure α-Fe_2O_3	2.200	–	Indirect (n = 2)	$(\alpha h\nu)^{1/2} = A(h\nu - E_g)$
α-Fe_2O_3–Co-300	1.773	19.4	Indirect (n = 2)	$(\alpha h\nu)^{1/2} = A(h\nu - E_g)$
α-Fe_2O_3–Co-550	1.180	46.4	Indirect (n = 2)	$(\alpha h\nu)^{1/2} = A(h\nu - E_g)$

the observed band gap narrowing. Collectively, these results suggest that both electronic interaction and structural strain play decisive roles in governing the optical response of Co-incorporated α-Fe_2O_3 systems.

EDX analysis

The data presented in the accompanying Table 5 elucidates the results derived from a meticulous elemental composition analysis, expressed in terms of percentage atomic composition, of two distinct types of α-Fe_2O_3-based photocatalysts that have been doped with Co and subjected to two different calcination temperatures, specifically 300 °C for the sample designated as α-Fe_2O_3-Co-300 and 550 °C for the sample labeled as α-Fe_2O_3-Co-550. The elemental analysis encompasses the assessment of various elements, including oxygen (O), iron (Fe), cobalt (Co), and silicon (Si), alongside the metal ratio of Fe to Co. Notably, at the lower calcination temperature of 300 °C, the concentration of Fe was recorded at 48.57%, which is significantly higher in comparison to the 40.30% observed at the elevated temperature of 550 °C. Conversely, the concentration of Co exhibited an upward trend, rising from 16.06% at 300 °C to 20.69% at 550 °C. The O content remained relatively stable, with values of 31.31 and 31.77% recorded for the two temperatures, respectively. This trend suggests that as the calcination temperature increases, there is a tendency for a decrease in Fe content alongside an increase in Co content within the material matrix. The elevation of the calcination temperature facilitates the more effective diffusion of Co ions into the α-Fe_2O_3 structure, thereby resulting in an increase in the integrated Co content within the matrix. In contrast, the available Fe content diminishes due to partial substitution by Co ions. Previous studies investigating transition metal-doped α-Fe_2O_3 materials have corroborated these findings, demonstrating that elevated calcination temperatures significantly enhance the diffusion and substitution of metal ions, thereby altering the overall composition and metal ratios within the synthesized materials [28].

Table 5. Elemental composition analysis by EDX

Sample	wt.%				Metal ratio
	O	Fe	Co	Si	
α-Fe_2O_3-Co-300	31.31	48.57	16.06	4.07	3:1
α-Fe_2O_3-Co-550	31.77	40.30	20.69	7.24	2:1

Moreover, it was observed that the Si content increased from 4.07% at 300 °C to 7.24% at 550 °C, which may be attributed to contamination from the synthesis equipment, the substrate used, or additional materials, such as silica, that were incorporated during the synthesis process. The presence of trace amounts of Si is frequently reported in the synthesis protocols for Fe_2O_3-based materials, and these small quantities of Si can play a beneficial role by acting as a structural support or enhancing the thermal stability of the resultant material [41]. The significance of the metal ratio cannot be overstated, as it plays a crucial role in dictating the photocatalytic properties of the material under investigation. The incorporation of Co into the α-Fe_2O_3 matrix has been shown to enhance photocatalytic activity by broadening the range of light absorption and improving the separation of charge carriers. However, it is imperative to recognize that an excessively high Co to Fe ratio may lead to adverse effects, such as the emergence of new phases or metal segregation, which could ultimately diminish the material's photocatalytic efficacy.

In conclusion, the simultaneous increase in Co content and the alteration of the Fe:Co ratio at elevated calcination temperatures generally serve to enhance the photocatalytic activity of α-Fe_2O_3, given that Co can function as a novel active center that promotes efficient electron transfer processes. Additionally, the progressive increase in Si content may contribute positively to the thermal and structural stability of the synthesized material. While higher calcination temperatures are conducive to the diffusion and incorporation of Co into the α-Fe_2O_3 framework, it is crucial to optimize these conditions carefully to avert issues such as metal segregation or the formation of undesired phases that could compromise the intended properties of the photocatalyst.

Photodegradation of MB

Lower calcination temperatures, specifically those around 300 °C, have been observed to result in the production of particulate matter with notably smaller dimensions and a significantly larger surface area. This phenomenon, in turn, effectively enhances the active surface area available for undergoing photocatalytic reactions, thereby facilitating a more efficient catalytic process. Conversely, when subjected to elevated calcination temperatures, such as 550 °C, there is a tendency for grain growth to occur, leading to a reduction in the active surface area and subsequently impairing the degradation efficiency of the photocatalytic activity. An increased surface area is crucial, as it amplifies the number of active sites present on the photocatalyst's surface, allowing a greater number of pollutant molecules to interact with the active radicals generated during the reaction. At the optimal calcination temperature of 300 °C, Co can be incorporated into the α-Fe_2O_3 structure in a more homogeneous and efficient manner as a dopant, without the risk of forming secondary phases or experiencing excessive agglomeration of Co particles. This optimal distribution of Co enhances the separation of electron-hole pairs, significantly decreasing the likelihood of recombination events and thereby improving the overall degradation efficiency of the photocatalytic process.

In contrast, at elevated calcination temperatures, it is possible for Co dopants to undergo phenomena such as segregation or the formation of new phases that exhibit diminished photocatalytic activity, which can adversely affect the degradation process. The comparison of the Fe:Co ratios in the samples α-Fe_2O_3-Co-300 (with a ratio of 3:1) and α-Fe_2O_3-Co-550 (with a ratio of 2:1) reveals that the doping of Co is still within an optimal range in the latter, as excessive doping, characterized by a lower ratio, can create centers for the recombination of electron-hole pairs that ultimately detract from the photocatalytic activity of the material. Furthermore, the degradation efficiency results of pure α-Fe_2O_3 without Co doping demonstrate that undoped α-Fe_2O_3 exhibits a significantly lower efficiency compared to both Co-doped samples (Fig. 5). This finding confirms the role of Co incorporation in enhancing the photocatalytic performance of the material.

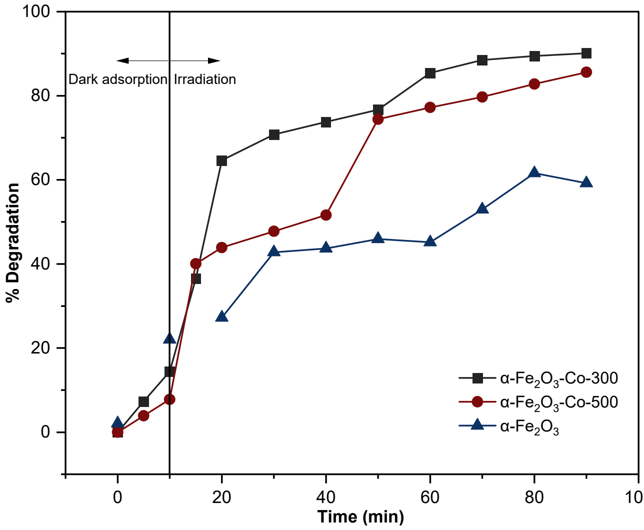

Fig 5. Effect of contact time on MB's degradation efficiency

The mechanism underlying the photocatalytic degradation processes involving α-Fe_2O_3-Co comprises multiple sequential stages; initially, α-Fe_2O_3 effectively absorbs visible light, which energizes electrons, allowing them to transition from the valence band to the conduction band. This energetic transition generates pairs of electrons (e^-) and holes (h^+) (Eq. (1)), which are crucial for subsequent reactions. The Co^{3+}/Co^{2+} ions present within the structure serve a vital role as centers for electron trapping, which significantly prolongs the lifespan of the generated electron-hole pairs, diminishes the rates of recombination, and enhances the overall charge transfer processes. The trapped electrons then engage in reactions with dissolved oxygen, leading to the formation of superoxide radicals ($\bullet O_2^-$) (Eq. (2)). Meanwhile, the holes participate in reactions with water molecules or hydroxide ions, generating highly reactive •OH (Eq. (3)). Both of these processes are instrumental in the degradation of organic pollutants. These active radicals effectively target and attack pollutant molecules, facilitating their breakdown into simpler and less harmful byproducts (Eq. (4)), thereby contributing to the overall efficiency of the photocatalytic process.

$$\alpha-Fe_2O_3-Co+h\nu \rightarrow e^- + h^+ \tag{1}$$

$$e^- + O_2 \rightarrow \bullet O_2^- \tag{2}$$

$$h^+ + H_2O/OH^- \rightarrow \bullet OH \tag{3}$$

$$\bullet O_2^-/{-OH} + \text{polutant} \rightarrow \text{degradation product} \tag{4}$$

Table 6. Kinetic parameters of α-Fe_2O_3-Co at various calcination temperatures based on pseudo-first- and pseudo-second-order models

Sample	Pseudo-first-order		Pseudo-second-order	
	k_1 (min^{-1})	R^2	k_2 (g mg^{-1} min^{-1})	R^2
α-Fe_2O_3-Co-300	0.01116	0.9651	2.13363	0.2157
α-Fe_2O_3-Co-550	0.00938	0.9206	3.31527	0.2216

The catalytic degradation kinetics of MB over α-Fe_2O_3-Co photocatalysts synthesized at varying calcination temperatures were evaluated using pseudo-first-order and pseudo-second-order kinetic models (Table 6). Based on the correlation coefficients (R^2), the pseudo-first-order model exhibited superior agreement with the experimental data, with R^2 values of 0.9651 for α-Fe_2O_3-Co-300 and 0.9206 for α-Fe_2O_3-Co-550. In contrast, the pseudo-second-order model demonstrated significantly lower R^2 values (0.2157 and 0.2216, respectively), indicating poor fit to the observed kinetic behavior. These results suggest that the photocatalytic degradation process is predominantly governed by a first-order reaction mechanism, in which the rate-limiting step likely involves the interaction between photogenerated reactive species (e.g., •OH) and dye molecules, rather than complex surface-controlled or multi-site chemisorption processes.

Moreover, the rate constant values (k_1) derived from the pseudo-first-order model show a slight decline with increasing calcination temperature, implying that excessive thermal treatment may reduce the density of catalytically active sites or alter the surface electronic structure, thereby diminishing reaction efficiency [42]. Although the pseudo-second-order rate constants (k_2) appear numerically larger, the associated low correlation values suggest that these may be mathematical artifacts with limited physical relevance in describing the degradation pathway [43]. The overall dominance of pseudo-first-order kinetics is consistent with previous reports on photocatalytic systems involving iron oxide composites, further supporting the role of photogenerated charge carriers and their reaction with dye molecules as the primary pathway for degradation. These findings highlight the significance of thermal process optimization in enhancing photocatalyst reactivity by striking an optimal balance between crystallinity, surface area, and active site availability.

■ CONCLUSION

This study concludes that Fe_2O_3-incorporated Co photocatalysts synthesized via a gelatin-modified silica hard-template method and calcined at varying temperatures exhibit distinct structural and photocatalytic characteristics that are directly influenced by thermal treatment. XRD and FTIR results confirmed improved crystallinity and the emergence of Co–O vibrational modes at higher temperatures, particularly in the α-Fe_2O_3–Co–550 sample, which also showed a shift in Fe:Co atomic ratio from 3:1 to 2:1 as revealed by EDX. Although BET analysis indicated a decline in surface area and pore volume with increasing calcination temperature, the α-Fe_2O_3–Co–550 catalyst achieved superior methylene blue degradation efficiency (> 90%) within 90 min, emphasizing the role of crystallographic and electronic factors over textural parameters alone. Kinetic evaluation demonstrated a better fit with the pseudo-first-order model for both samples, with slightly higher rate constants for α-Fe_2O_3–Co–300; however, this did not directly correlate with overall degradation performance. These findings underscore the synergistic effect of cobalt incorporation, controlled crystallization, and template-assisted porosity in enhancing charge separation and photocatalytic reactivity, offering a rational design route for high-performance photocatalysts in wastewater treatment applications.

■ ACKNOWLEDGMENTS

This research was funded by the *Penelitian Unggulan Terapan A (PUTA)* scheme under Sebelas Maret University through research contract number 369/UN27.22/PT.01.03/2025. The authors gratefully acknowledge the financial support and research facilities provided by Sebelas Maret University (UNS), Surakarta, Indonesia.

CONFLICT OF INTEREST

The authors declare no conflict of interest.

AUTHOR CONTRIBUTIONS

Maria Ulfa: Conceptualization, Funding acquisition, Methodology, Investigation, Writing – Original Draft, Writing – Review & Editing, Supervision. Istinganah Saestu Rohmah: Formal analysis, Software, Validation, Writing – Review & Editing. Both authors have read and agreed to the final version of the manuscript.

REFERENCES

[1] Mulushewa, Z., Dinbore, W.T., and Ayele, Y., 2021, Removal of methylene blue from textile waste water using kaolin and zeolite-x synthesized from Ethiopian kaolin, *Environ. Anal. Health Toxicol.*, 36 (1), e2021007.

[2] Oladoye, P.O., Ajiboye, T.O., Omotola, E.O., and Oyewola, O.J., 2022, Methylene blue dye: Toxicity and potential elimination technology from wastewater, *Results Eng.*, 16, 100678.

[3] Sarkar Phyllis, A.K., Tortora, G., and Johnson, I., 2022, "Photodegradation" in *The Fairchild Books Dictionary of Textiles*, Bloomsbury Publishing Inc., New York, NY, US, 340–345.

[4] Katheresan, V., Kansedo, J., and Lau, S.Y., 2018, Efficiency of various recent wastewater dye removal methods: A review, *J. Environ. Chem. Eng.*, 6 (4), 4676–4697.

[5] Essa, W.K., 2024, Methylene blue removal by copper oxide nanoparticles obtained from green synthesis of melia azedarach: Kinetic and isotherm studies, *Chemistry*, 6 (1), 249–263.

[6] Krishna Moorthy, A., Govindarajan Rathi, B., Shukla, S.P., Kumar, K., and Shree Bharti, V., 2021, Acute toxicity of textile dye methylene blue on growth and metabolism of selected freshwater microalgae, *Environ. Toxicol. Pharmacol.*, 82, 103552.

[7] Peng, X., Jiang, Y., Chen, Z., Osman, A.I., Farghali, M., Rooney, D.W., and Yap, P.S., 2023, Recycling municipal, agricultural and industrial waste into energy, fertilizers, food and construction materials, and economic feasibility: A review, *Environ. Chem. Lett.*, 21 (2), 765–801.

[8] Ulusoy, A., Atılgan, A., Rolbiecki, R., Jagosz, B., and Rolbiecki, S., 2024, Innovative approaches for sustainable wastewater resource management, *Agriculture*, 14 (12), 2111.

[9] Ramesh, N., Lai, C.W., Johan, M.R.B., Mousavi, S.M., Badruddin, I.A., Kumar, A., Sharma, G., and Gapsari, F., 2024, Progress in photocatalytic degradation of industrial organic dye by utilising the silver doped titanium dioxide nanocomposite, *Heliyon*, 10 (24), e40998.

[10] Dostanić, J., Lončarević, D., Hadnađev-Kostić, M., and Vulić, T., 2024, Recent advances in the strategies for developing and modifying photocatalytic materials for wastewater treatment, *Processes*, 12 (9), 1914.

[11] Pavel, M., Anastasescu, C., State, R.N., Vasile, A., Papa, F., and Balint, I., 2023, Photocatalytic degradation of organic and inorganic pollutants to harmless end products: Assessment of practical application potential for water and air cleaning, *Catalysts*, 13 (2), 380.

[12] Rashid, R., Shafiq, I., Gilani, M.R.H.S., Maaz, M., Akhter, P., Hussain, M., Jeong, K.E., Kwon, E.E., Bae, S., and Park, Y.K., 2024, Advancements in TiO_2-based photocatalysis for environmental remediation: Strategies for enhancing visible-light-driven activity, *Chemosphere*, 349, 140703.

[13] Kumar, Y., Kumar, R., Raizada, P., Khan, A.A.P., Singh, A., Le, Q.V., Nguyen, V.H., Selvasembian, R., Thakur, S., and Singh, P., 2022, Current status of hematite (α-Fe_2O_3) based Z-scheme photocatalytic systems for environmental and energy applications, *J. Environ. Chem. Eng.*, 10 (3), 107427.

[14] Keerthana, S.P., Yuvakkumar, R., Ravi, G., Kumar, P., Elshikh, M.S., Alkhamis, H.H., Alrefaei, A.F., and Velauthapillai, D., 2021, A strategy to enhance the photocatalytic efficiency of α-Fe_2O_3, *Chemosphere*, 270, 129498.

[15] Liu, X., Lu, Q., Zhu, C., and Liu, S., 2015, Enhanced photocatalytic activity of α-Fe_2O_3/Bi_2WO_6 heterostructured nanofibers prepared by

electrospinning technique, *RSC Adv.*, 5 (6), 4077–4082.

[16] Zhang, Y.J., He, P.Y., Zhang, Y.X., and Chen, H., 2018, A novel electroconductive graphene/fly ash-based geopolymer composite and its photocatalytic performance, *Chem. Eng. J.*, 334, 2459–2466.

[17] Kumar, A., Trivedi, S.K., Phor, L., Malik, J., Bhargava, S., Kaushik, V., Kumar, P., and Chahal, S., 2023, Visible light activated Mg, Co co-doped hematite for effective removal of reactive red 35 from textile wastewater, *Ceram. Int.*, 49 (23, Pt. A), 37691–37699.

[18] Subudhi, S., Mahapatra, A., Mandal, M., Das, S., Sa, K., Alam, I., Subramanyam, B.V.R.S., Raiguru, J., and Mahanandia, P., 2020, Effect of Co doping in tuning the band gap of $LaFeO_3$, *Integr. Ferroelectr.*, 205 (1), 61–65.

[19] Yang, F., Yang, L., Ai, C., Xie, P., Lin, S., Wang, C.Z., and Lu, X., 2018, Tailoring bandgap of perovskite $BaTiO_3$ by transition metals co-doping for visible-light photoelectrical applications: A first-principles study, *Nanomaterials*, 8 (7), 455.

[20] Wang, J., Li, P., Zhao, Y., and Zeng, X., 2022, Nb/N co-doped layered perovskite Sr_2TiO_4: Preparation and enhanced photocatalytic degradation tetracycline under visible light, *Int. J. Mol. Sci.*, 23 (18), 10927.

[21] Ulfa, M., Rohmah, I.S., and Anggreani, C.N., 2025, Driving photocatalytic efficiency through controlled cobalt–iron and cobalt–nickel ratios for methylene blue degradation, *Bull. Chem. React. Eng. Catal.*, 20 (4), 607–623.

[22] do Carmo Batista, W.V.F., da Cunha, R., de Oliveira, W.L., da Cruz, T.S., Gorgulho, H.F., dos Reis Ferreira, R.A., Pereira, M.C., and Mesquita, J.P., 2025, Improved dye adsorption and photodegradation using mesoporous carbon modified with titania and magnetic nanoparticles, *Results Surf. Interfaces*, 19, 100532.

[23] Dziewiątka, K., Matusik, J., Trenczek-Zając, A., and Cempura, G., 2023, TiO_2-loaded nanotubular kaolin group minerals: The effect of mineral support on photodegradation of dyes as model pollutants, *Appl. Clay Sci.*, 245, 107123.

[24] Khalaf, A., Abu-Dalo, D., and Alshamaileh, E., 2024, Synthesis, characterization, and application of Fe_2O_3 nanophotocatalyst for the treatment of various pollutants in aqueous phase: A systematic review, *Sci. World J.*, 2024 (1), 8644322.

[25] Purnama, B., Wijayanta, A.T., and Suharyana, S., 2019, Effect of calcination temperature on structural and magnetic properties in cobalt ferrite nano particles, *J. King Saud Univ. - Sci.*, 31 (4), 956–960.

[26] Prabhakaran, T., Mangalaraja, R.V., Denardin, J.C., and Jiménez, J.A., 2017, The effect of calcination temperature on the structural and magnetic properties of co-precipitated $CoFe_2O_4$ nanoparticles, *J. Alloys Compd.*, 716, 171–183.

[27] Rostas, A.M., Suciu, R.C., Roşu, M.C., Turza, A., Cosma, D.V., Tripon, S., Fort, C.I., Danciu, V., Baia, M., Bocirnea, A., and Indrea, E., 2025, Annealing temperature, a key factor in shaping Ag-decorated TiO_2 aerogels as efficient visible-light photocatalysts, *Mater. Chem. Phys.*, 337, 130557.

[28] Ulfa, M., and Lestari, S., 2025, Design of bi- and tri-metal oxide photocatalysts via gelatin-directed mesoporous silica hard templating for advanced dye degradation, *Bull. Chem. React. Eng. Catal.*, 20 (4), 661–671.

[29] Jdidi, A.R., Nouira, W., Selmi, A., Drissi, N., Aissa, M., Hcini, S., and Gassoumi, M., 2025, Impact of calcination temperature on the properties and photocatalytic efficiency of $Cd_{0.6}Mg_{0.2}Cu_{0.2}Fe_2O_4$ spinel ferrites synthesized via the sol–gel method, *Crystals*, 15 (5), 457.

[30] Xie, T., Liu, Y., Wang, H., and Wu, Z., 2019, Synthesis of α-Fe_2O_3/Bi_2WO_6 layered heterojunctions by *in situ* growth strategy with enhanced visible-light photocatalytic activity, *Sci. Rep.*, 9 (1), 7551.

[31] Deon, F., Koch-Müller, M., Rhede, D., Gottschalk, M., Wirth, R., and Thomas, S.M., 2010, Location and quantification of hydroxyl in wadsleyite: New insights, *Am. Mineral.*, 95 (2-3), 312–322.

[32] Ulfa, M., and Rohmah, I.S., 2025, Thermal-induced structural evolution of mesoporous oxides Fe–Co–

Ni for enhanced visible-light dye degradation, *Next Mater.*, 9, 101024.

[33] Wu, L., Wang, W., Zhang, S., Mo, D., and Li, X., 2021, Fabrication and characterization of Co-doped Fe_2O_3 spindles for the enhanced photo-Fenton catalytic degradation of tetracycline, *ACS Omega*, 6 (49), 33717–33727.

[34] Amiruddin, E., Awaluddin, A., Rini, A.S., Umar, L., Rianna, M., Hadilala, T.P., and Putri, N., 2024, Magnetic and optical properties of a-Fe_2O_3/TiO_2 nanocomposite derived from Logas natural sand for environmental application, *J. Phys. Conf. Ser.*, 2908 (1), 012003.

[35] Zain, M., Yasin, K.A., Haq, S., Rehman, W., Din, S.U., Shujaat, S., Syed, A., Hossain, M.K., Paray, B.A., Razzokov, J., and Samad, A., 2024, Effect of calcination temperature induced structural modifications on the photocatalytic efficacy of Fe_2O_3-ZrO_2 nanostructures: mechanochemical synthesis, *RSC Adv.*, 14 (21), 15085–15094.

[36] Li, Y., Ren, Z., He, Z., Ouyang, P., Duan, Y., Zhang, W., Lv, K., and Dong, F., 2024, Crystallinity-defect matching relationship of g-C_3N_4: Experimental and theoretical perspectives, *Green Energy Environ.*, 9 (4), 623–658.

[37] Zemlik, M., Białobrzeska, B., Stachowicz, M., and Hanszke, J., 2024, The influence of grain size on the abrasive wear resistance of Hardox 500 steel, *Appl. Sci.*, 14 (24), 11490.

[38] Gareev, K.G., 2023, Diversity of iron oxides: mechanisms of formation, physical properties and applications, *Magnetochemistry*, 9 (5), 119.

[39] Zhao, Q., Tang, Q., Chu, H., Pan, Z., Pan, H., Zhao, S., and Li, D., 2025, Ultra-high temperature calcination of crystalline α-Fe_2O_3 and its nonlinear optical properties for ultrafast photonics, *Adv. Sci.*, 12 (18), 2500896.

[40] Jiang, S., You, Z., and Tang, N., 2023, Effects of calcination temperature and calcination atmosphere on the performance of Co_3O_4 catalysts for the catalytic oxidation of toluene, *Processes*, 11 (7), 2087.

[41] Sani, A., and Dahman, Y., 2010, Improvements in the production of bacterial synthesized biocellulose nanofibres using different culture methods, *J. Chem. Technol. Biotechnol.*, 85 (2), 151–164.

[42] Khanam, J., Hasan, M.R., Biswas, B., Ahmed, M.F., Mostofa, S., Akhtar, U.S., Hossain, M.K., Quddus, M.S., Ahmed, S., Sharmin, N., and Al-Reza, S.M., 2024, Effect of low temperature calcination on micro structure of hematite nanoparticles synthesized from waste iron source, *Heliyon*, 10 (24), e41030.

[43] Bullen, J.C., Saleesongsom, S., Gallagher, K., and Weiss, D.J., 2021, A revised pseudo-second-order kinetic model for adsorption, sensitive to changes in adsorbate and adsorbent concentrations, *Langmuir*, 37 (10), 3189–3201.